Effects of Strain Rate on the TRIP–TWIP Transition of an Austenitic Fe-18Mn-2Si-2Al Steel

M. RAPOSO, M. MARTÍN, M.F. GIORDANA, V. FUSTER, and J. MALARRÍA

A fully austenitic Fe-18Mn-2Si-2Al transformation-induced plasticity (TRIP) steel was tensile tested from quasi-static to low-dynamic regime at three different strain rates: 4.7×10^{-4}, 1.3×10^{-1}, and 8.3×10^{0} s^{-1}. Typical two-stage transformation mechanism, TRIP $\gamma \rightarrow \varepsilon \rightarrow \alpha'$, was observed for samples tested at 4.7×10^{-4} s^{-1}. At higher strain rates, the increase in temperature due to adiabatic plastic work shifts the stacking fault energy (SFE) towards a twinning-induced plasticity–SFE-range modifying the mechanical behavior of the alloy. This change on the deformation mechanism leads to a lower work hardening capacity and a higher elongation to rupture in samples tested at 1.3×10^{-1} and 8.3×10^{0} s^{-1}. In this context, the alloy maintains its energy absorption capability with a maximum reduction of 3.6 pct according to the Rm $\times$ A parameter. The Md temperature, experimentally determined in the present study, proved to be a useful tool for understanding the material's behavior.

https://doi.org/10.1007/s11661-019-05331-9

I. INTRODUCTION

THE need of reducing greenhouse gases emissions and controlling global warming has pushed the development of alloys with reduced specific weight for structural uses. Particularly, the automotive industry leads this field by introducing new steels which allow a reduction of fuel consumption and simultaneously improve human safety in a crash event. High-manganese transformation-induced plasticity (HMn-TRIP) steels belong to this category of advanced high-strength automotive steels. HMn-TRIP steels combine high strength and ductility, excellent formability, superior fracture toughness, and reduced specific weight due to the incorporation of lighter substitutional elements.[1–5] Such elements are manganese, silicon, and aluminum all of them carrying an alloying purpose besides reducing specific weight.

The content of manganese in HMn-TRIP steels varies between 15 and 30 wt pct with the aim of stabilizing the austenite-fcc phase. Silicon and aluminum are incorporated in amounts close to 3 wt pct for controlling the stacking fault energy (SFE) of the alloy. In this range of composition, HMn-TRIP steels present a metastable γ-austenite (fcc) which transforms to ε-martensite (hcp) and to α'-martensite (bcc) when an external mechanical stress is applied. This strain-induced transformation can follow two possible paths: a $\gamma \rightarrow \alpha'$ single-stage, or a two-stage $\gamma \rightarrow \varepsilon \rightarrow \alpha'$ transformation in which the ε-martensite acts as an intermediate phase.[6–12]

Tensile properties of HMn-TRIP steels and the occurring deformation mechanism will depend on the SFE of the alloy which in turn is determined by the chemical composition. Three levels on SFE are recognized to promote either transformation-induced plasticity (TRIP effect), twinning-induced plasticity (TWIP effect), or dislocation glide, at SFE < 18 mJ/m^{-2}, $18 <$ SFE < 45 mJ/m^{-2}, and SFE > 45 mJ/m^{-2}, respectively.[13–16] Therefore, the SFE is a fundamental parameter to be considered at the time of defining a novel composition.

Since these types of steels are meant to be part of the car body structure, it is mandatory to assess the mechanical behavior under different strain rates. Part of this work has been done by Frommeyer *et al.*, Grässel *et al.*, and more recently by Benzing *et al.*[3–5,17] They have shown that increasing strain rates lead to a higher yield strength, an increase in the amount of post-uniform elongation, and a significant rise on the temperature of the tensile specimen. In this framework, fewer analyses are found concerning the energy absorption capability (EAC) of the alloys when the loading condition varies by several orders of magnitude in terms of strain rate.

This work introduces an austenitic HMn-TRIP steel which combines high ductility and high EAC along a wide strain rate regime. From the compositional point

M. RAPOSO, M. MARTÍN, M.F. GIORDANA, V. FUSTER, and J. MALARRÍA are with the Instituto de Física Rosario (CONICET-UNR), Bv. 27 de Febrero 210 bis, Rosario, Argentina. Contact e-mail: raposo@ifir-conicet.gov.ar

Manuscript submitted April 4, 2019.

Published online: 25 June 2019

of view, an austenitic matrix is achieved with a relatively "low" manganese content in comparison with other alloys of the family of HMn-TRIP steels. Simultaneously, silicon and aluminum are also reduced giving an adjusted composition of Fe-18Mn-2Si-2Al, with a nominal carbon content of 0.05 wt pct. The alloy was tensile tested from a quasi-static, 10^{-4} s^{-1}, to a low-dynamic, 10^{1} s^{-1}, strain rate condition. Such evaluation indicates that the TRIP effect diminishes with increasing strain rates. It is shown that the change in the deformation mode is related to an increase of the specimen's temperature which is high enough to modify the SFE of the alloy, and even overcome the corresponding Md temperature. Despite the modification of the dominant deformation mechanism, the material conserves its EAC assessed by the product of the ultimate tensile strength and the total elongation to rupture.

II. MATERIALS AND EXPERIMENTAL PROCEDURES

A. *Material and Specimen Preparation*

The alloy was produced in our laboratory *via* ingot casting in an induction furnace under reducing atmosphere. The as-cast ingots with a dimension of $130 \times 60 \times 11$ mm^3 were pre-machined and hot-rolled at 1050 °C in several passes to 2-mm-thick sheets. Subsize tensile specimens with 16 mm gauge length and 6 mm wide were cut from the steel sheets *via* electrical discharge machining according to ASTM-E 8M standard. The tensile specimens were solution annealed at 1050 °C during 15 minutes under protective atmosphere and cooled down under calm air to room temperature, hereinafter referred as *starting condition*. Chemical composition was measured by means of optical emission spectroscopy, see Table I. Optical microscopy (OM) samples of 6×6 mm^2 were cut from the specimens and polished following standard metallographic procedures up to 1 μm diamond paste. The etching was performed using 2 pct Nital solution. The OM images were processed with the software ImageJ for evaluating the mean grain size using the linear intercept method.

B. *Mechanical Properties and Microstructure*

In order to determine mechanical properties and microstructure evolution as function of the strain, uniaxial tensile tests were conducted on a 100 kN MTS-810 Servo Hydraulic Machine, at three different crosshead speeds: 0.45, 120, and 8000 mm/min. These values correspond to an initial strain rate of 4.7×10^{-4}, 1.3×10^{-1}, and 8.3×10^{0} s^{-1} respectively; hereinafter referred as 10^{-4}, 10^{-1}, and 10^{1} s^{-1}, for the sake of simplicity. In all cases, the laboratory was conditioned to a 22 °C room temperature.

X-ray diffraction (XRD) patterns were measured using Cu $K\alpha_1/K\alpha_2$ lines in a PANalytical Empyrean X-ray diffractometer operating at 40 kV and 40 mA. The scans were collected from 35 deg to 105 deg, with 0.013 deg step size, and 108.12 seconds time per step. The instrumental standard chosen to account for instrumental broadening was silicon. XRD samples were subjected to an electropolishing process employing a solution of 800 mL of acetic acid and 200 mL of perchloric acid at 20 V and 25 °C. X-ray characterization of each sample was performed by Rietveld refinement of the corresponding patterns, using the Java-based software Maud (Materials Analysis using Diffraction) version 2.79 released November 3, 2017.[18,19] To account for texture effects, the intensity correction of the X-ray patterns was done using the harmonic texture model implemented in Maud. In all cases, the estimated error for the amount of each phase is ± 2 pct.

Transmission electron microscope (TEM) microstructural analyses were performed using a JEOL JEM-2100 plus scanning-TEM (STEM) operated at 200 kV. TEM specimens were electropolished using a double-jet TENUPOL 5 equipment. A solution of 900 mL ethanol and 100 mL perchloric acid was used as electrolyte at – 11 °C and 20.5 V.

C. *Md and In Situ Temperature Determination*

In order to determine Md temperature of the alloy, mechanical testing was performed by using an INSTRON 3362 electromechanical testing machine equipped with a temperature control device (range – 50 °C to 200 °C). Tensile specimens were tested using a crosshead speed of 0.45 mm/min at different temperatures between − 30 and 100 °C, and the yield stress of each one determined by the 0.2 pct offset method.

Temperature rise in tensile specimens due to the strain rate was acquired *in situ* by a digital multimeter employing spot-welded type-K thermocouples.

III. RESULTS

Figure 1 shows the optical micrograph of the Fe-18Mn-2Si-2Al alloy at starting condition according to Sect. 2.1. A fully austenitic γ (fcc) microstructure is observed, featuring an average grain size of 51 ± 5 μm (G-ASTM 5.5).

A series of loading–unloading tensile cycles were performed in order to assess the active deformation mechanism associated with phase transitions when the alloy is loaded in the quasi-static regime. Figure 2(a) shows the stress–strain curves obtained by cyclic loading and unloading steps. Right after unloading, the specimens were analyzed by XRD and returned to the tensile testing machine. The XRD measurements are shown in Figure 2(b). As a first result, the diffraction pattern (DP) corresponding to the starting condition, 0 pct engineering strain, confirms the fully austenitic state of the alloy before testing, in agreement with our OM observations (see Figure 1). According to Figure 2(b), ε-martensite (hcp) is the first to form as a result of the applied mechanical deformation, and after around 10 pct of engineering deformation the α'-martensite (bcc) reflections become noticeable. Rietveld refinement of the XRD patterns was done in order to estimate each phase

Table I. Chemical Composition Measured by Optical Emission Spectroscopy (Wt Pct)

Condition	Mn	Si	Al	C	Fe
15 min, 1050 °C, calm air cooling	18.3	2.1	1.9	0.04	bal.

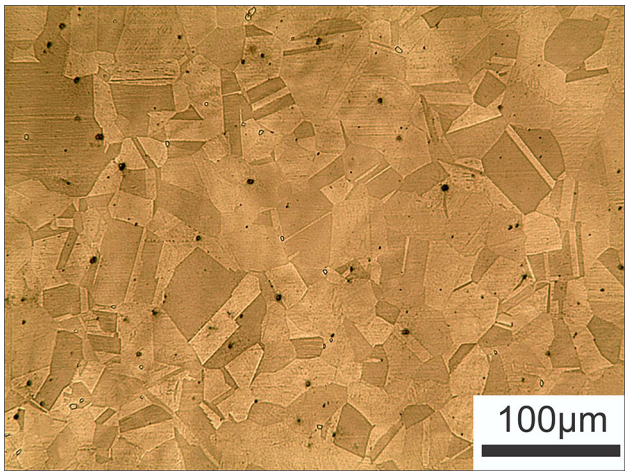

Fig. 1—Optical micrograph of the alloy, at starting condition, showing austenitic grains.

amount, so as to achieve a better resolution of the deformation mechanism, as depicted in Figure 3. A high-rate transformation of austenite into ε-martensite is observed at the early stages of deformation. In this way, the hcp phase reaches its maximum volume fraction at 11 pct of engineering strain, entering into a decaying process with further strain. On the other hand, the volume fraction of α′-martensite increases steadily throughout all the deformation process. At around 13 pct of engineering strain the austenitic and both martensitic phases coexist, with an almost equal volume fraction of 33 pct. Finally, the complete deformation process turns the bulk material into a multi-phase matrix composed of 88 pct α′-martensite, 6 pct ε-martensite, and 6 pct of non-transformed γ at the last cycle, where 40 pct of accumulated engineering strain is reached.

Figure 4 presents the engineering stress–strain curves of the Fe-18Mn-2Si-2Al alloy, measured on different specimens, at three levels of initial strain rate: 10^{-4}, 10^{-1}, and 10^{1} s^{-1}. Tensile properties at every testing condition are summarized in Table II. It can be seen that the 0.2 pct offset yield strength (Rp0.2) slightly increases with the strain rate. The maximum tensile strength (Rm) was registered for the quasi-static condition, 10^{-4} s^{-1}, with an average value of 837 MPa, being 115 MPa higher than those obtained at 10^{-1} and 10^{1} s^{-1}. On the contrary, the uniform elongation (Ag) of the 10^{-4} specimens is in average 4 pct lower than the 10^{-1} and 10^{1} specimens which reach an average value of 42 pct. The elongation to fracture (A) is also reduced by

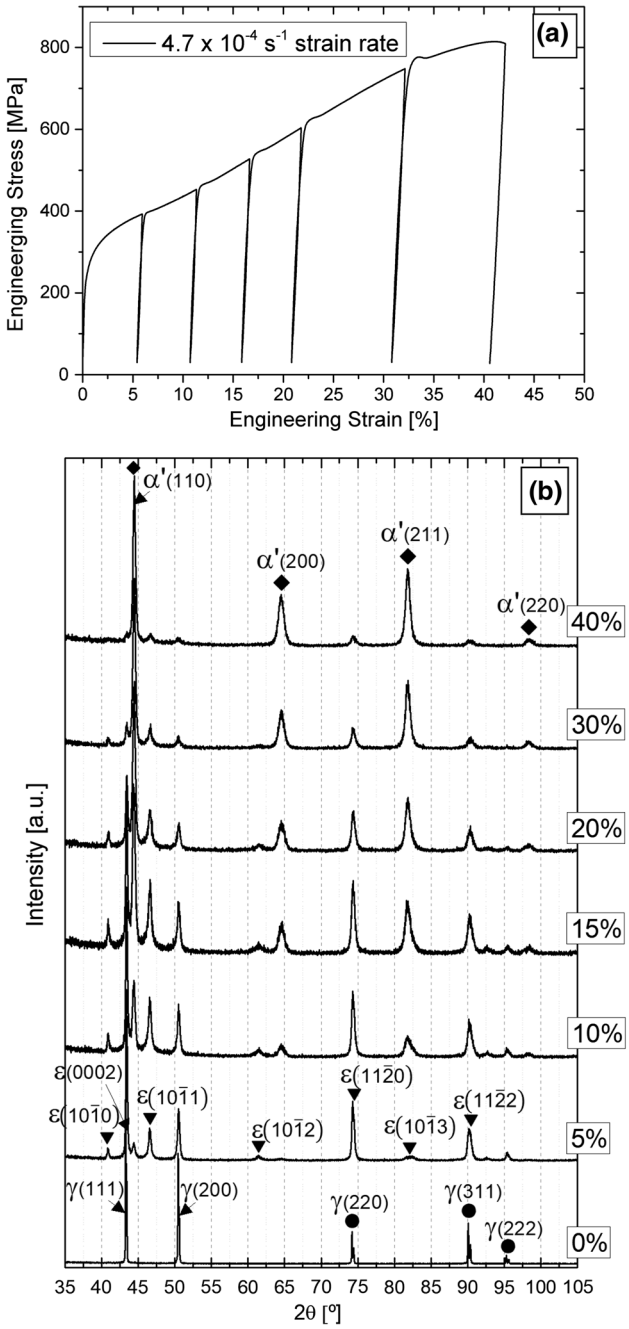

Fig. 2—Cyclic loading–unloading tensile testing of the same Fe-18Mn-2Si-2Al specimen, for microstructural evolution assessment, in the quasi-static regime. (*a*) Engineering stress–strain curves at quasi-static condition, 10^{-4} s^{-1} and (*b*) XRD patterns measured immediately after each tensile test, accounting for a total measuring time of 1 h.

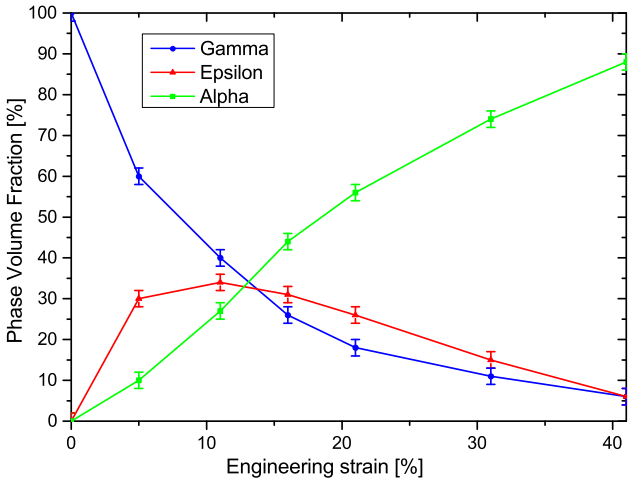

Fig. 3—Volume fraction of phases calculated by Rietveld refinement of the XRD spectra shown in Fig. 2(b).

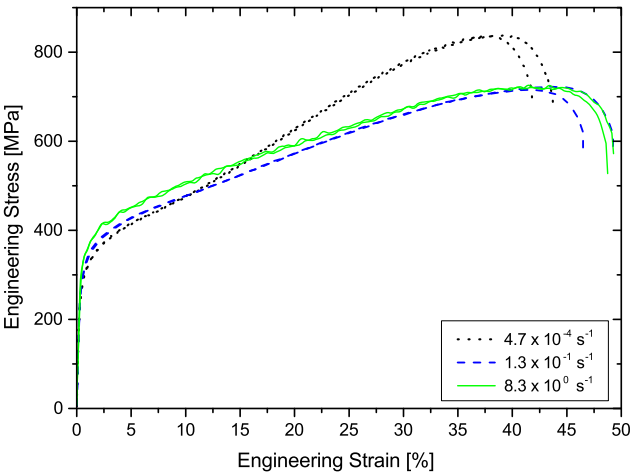

Fig. 4—Engineering stress–strain curves of specimens tested at 10^{-4}, 10^{-1}, and 10^{1} s^{-1}, up to failure, of the Fe-18Mn-2Si-Al alloy.

6 pct for the quasi-static condition in comparison to the 10^{-1} and 10^{1} strain rates.

Table II also presents the product between Rm and A which is representative of the EAC of the material. This calculation indicates that the highest EAC occurs for quasi-static loading, being 3.6 and 0.8 pct higher than the obtained for the 10^{-1} and 10^{1} s^{-1} testing conditions, respectively.

The evolution of the strain hardening exponent, n, at every strain rate level was obtained according to Hollomon's relationship, up to Rm, as follows[20]:

$$n = \frac{d(\ln \sigma_T)}{d(\ln \varepsilon_T)} \quad [1]$$

being σ_T the true stress and ε_T the true strain. Thus, the behavior of the n exponent is of main interest since it reflects in an indirect manner the intensity of the strain-induced transformation. Figure 5(a) depicts the n-exponent curves as function of engineering strain, with an adjacent averaging smoothing. Samples deformed at 10^{-4} s^{-1} achieve a maximum n of 0.83 at a middle deformation stage of 25 pct. After increasing the strain rate to 10^{-1} s^{-1}, there is a reduction in the n-maximum value to 0.63 at 25 pct engineering strain, which remains almost constant up to 36 pct. In the samples deformed at 10^{1} s^{-1} the maximum n value is also lower, $n = 0.65$, and it arises at a higher deformation stage, close to 32 pct strain.

A similar strain rate effect is observed in Figure 5(b) which represents the strain hardening rates curves, $d\sigma_T/d\varepsilon_T$, plotted as function of engineering strain and with an adjacent averaging smoothing. While typical structural metallic alloys present monotonous decay of the hardening rate with strain, Figure 5(b) shows the activation of a hardening process after the strain local minimum.[21] It can be seen that the 10^{-4} s^{-1} strain hardening rate curve initially decreases to a local minimum, at 7 pct strain, and subsequently increase to its maximum at 24 pct, where it starts decreasing. The first minimum for the 10^{-1} s^{-1} rate test is at 9 pct strain, and it reaches its highest strain hardening rate value at 26 pct strain. The 10^{1} s^{-1} curve remains almost constant from 9 pct up to 18 pct strain, before it starts increasing to its maximum, reached at 30 pct strain.

While Figures 5(a) and (b) give an impression on how fast the strain-induced transformation occurs along the tensile tests, Table III indicates directly the amount of the present phases in the specimens after rupture. As can be seen, the amount of non-transformed austenite increases with strain rate from 7 to 47 pct volume fraction between quasi-static-10^{-4} and low-dynamic-10^{1} s^{-1} conditions. In accordance with the matrix behavior, the volume fraction of α'-martensite after rupture decreases from 88 to 44 pct in the same range of strain rate.

Transmission and scanning electron microscopy analysis was performed in order to obtain a detailed microstructural characterization. EBSD micrograph of a sample deformed 11 pct at 10^{-4} s^{-1} is presented in Figure 6. It shows an austenitic matrix with ε-martensite plates, and lenticular α'-martensites inside the ε-plates.

TEM images and DPs were taken from annealed material and from specimens tested at the three strain rates used in this research. The microstructure of a solution-annealed sample (starting condition) comprises a fully austenitic matrix, in correspondence with light microscopy and XRD analysis. In Figures 7(a) and (b), the austenitic matrix is observed at the bright field image with a grain in [013]γ zone axis, and the occurrence of some stacking faults. Concerning tested specimens, all of them possess a common feature, consisting in large regions of α'-martensite (the volume fraction of the α'-martensite was quantitatively calculated by Rietveld refinement of the XRD spectra, and is listed in Table III). Such areas, where α'-martensite is observed, are characterized by a high dislocation density. In the specimens tested at 10^{-4} s^{-1} strain rate, the coexistence of ε-martensite and γ-austenite is observed by TEM, as shown in Figures 7(c) and (d). The specimens strained at 10^{-1} s^{-1} show an austenitic matrix characterized by the formation of very thin bands. In the associated DP, ε-martensite spots are found together with extra spots,

Table II. Mechanical Properties of the Fe-18Mn-2Si-2Al TRIP Steel at Different Strain Rates

Strain Rate (s^{-1})	Rp0.2 (MPa)	Rm (MPa)	Ag (Pct)	A (Pct)	Average Rm × A (MPa Pct)
4.7×10^{-4} (10^{-4})	269	836	37	41	35,239
	266	838	38	43	
1.3×10^{-1} (10^{-1})	293	723	43	49	33,942
	288	715	41	46	
8.3×10^{0} (10^{1})	325	725	43	49	34,946
	327	722	40	48	

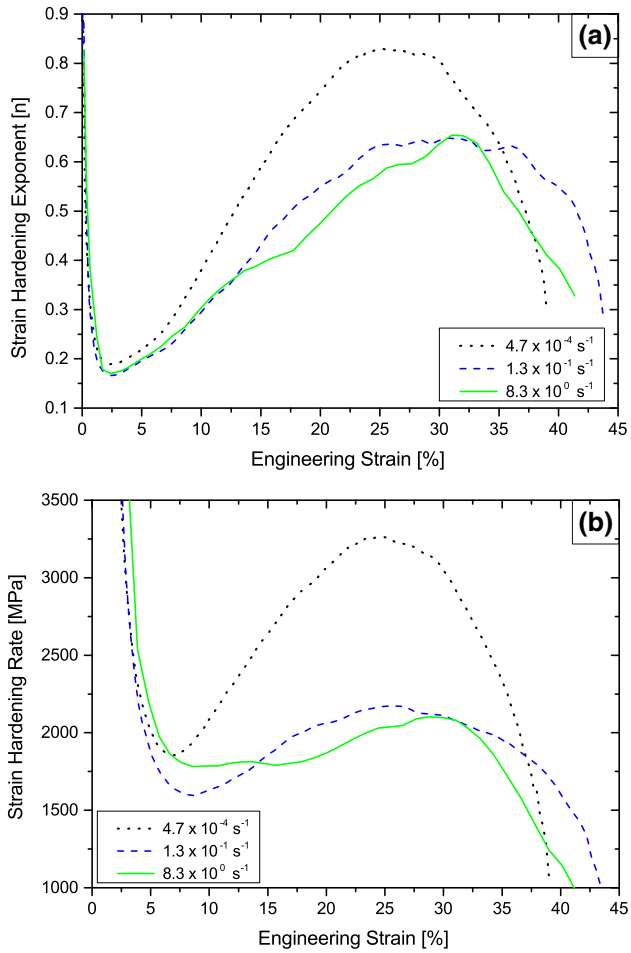

Fig. 5—Qualitative monitoring of TRIP effect, at the three initial strain rates. (*a*) Strain hardening exponent n and (*b*) strain hardening rate, $d\sigma_T/d\varepsilon_T$.

Table III. Volume Fraction of Phases After Rupture

Strain Rate (1/s)	γ (Pct ± 2)	ε (Pct ± 2)	α' (Pct ± 2)
4.7×10^{-4} (10^{-4})	7	5	88
1.3×10^{-1} (10^{-1})	31	8	61
8.3×10^{0} (10^{1})	47	9	44

which indicate the occurrence of twinning. This is shown in Figures 7(e) and (f), and reflect a mixed TRIP–TWIP regime already present for the 10^{-1} s^{-1} testing condition. For the 10^{1} s^{-1} strain rate, the microstructure is also formed by very thin bands, but no epsilon ε-martensite was found in the examined samples. The corresponding DP are indexed as a twinned austenitic matrix, as shown in Figures 7(g) and (h). This type of microstructure is in agreement with the observations of Kürnsteiner and Pramanik *et al.* where nanometric twins are reported.[22,23]

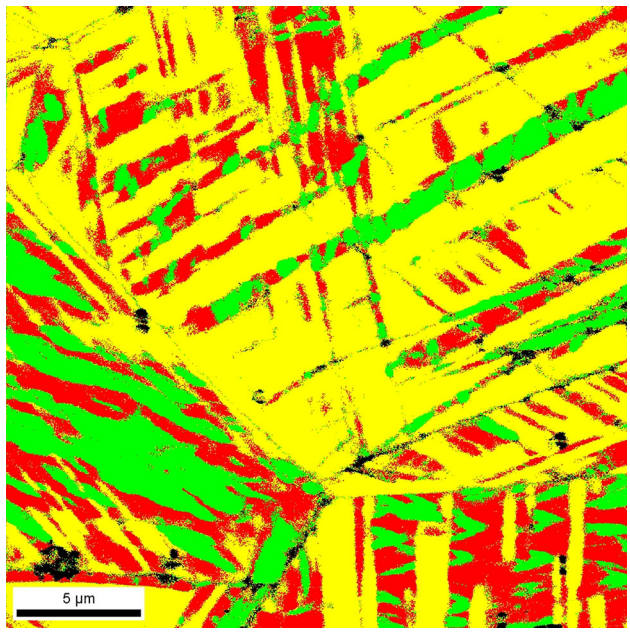

Fig. 6—Mapping of present phases obtained by electron backscatter diffraction (EBSD) at 11 pct of plastic deformation and quasi-static loading: austenite-yellow, ε-martensite-red, α'-martensite-green (Color figure online).

IV. DISCUSSION

The Fe-18Mn-2Si-2Al HMn-TRIP steel introduced in this work is characterized by a fully austenitic microstructure in the starting condition. This is confirmed *via* OM in Figure 1 and by the XRD pattern corresponding to null engineering strain in Figure 2(b). This initial microstructure differs from most of HMn-TRIP steels developed in the Fe-Mn-Si-Al system. Representative compositions featuring a mixed starting microstructure are for instance the Fe-15Mn-3Si-3Al and Fe-20Mn-3Si-3Al produced by Frommeyer *et al.*[5]

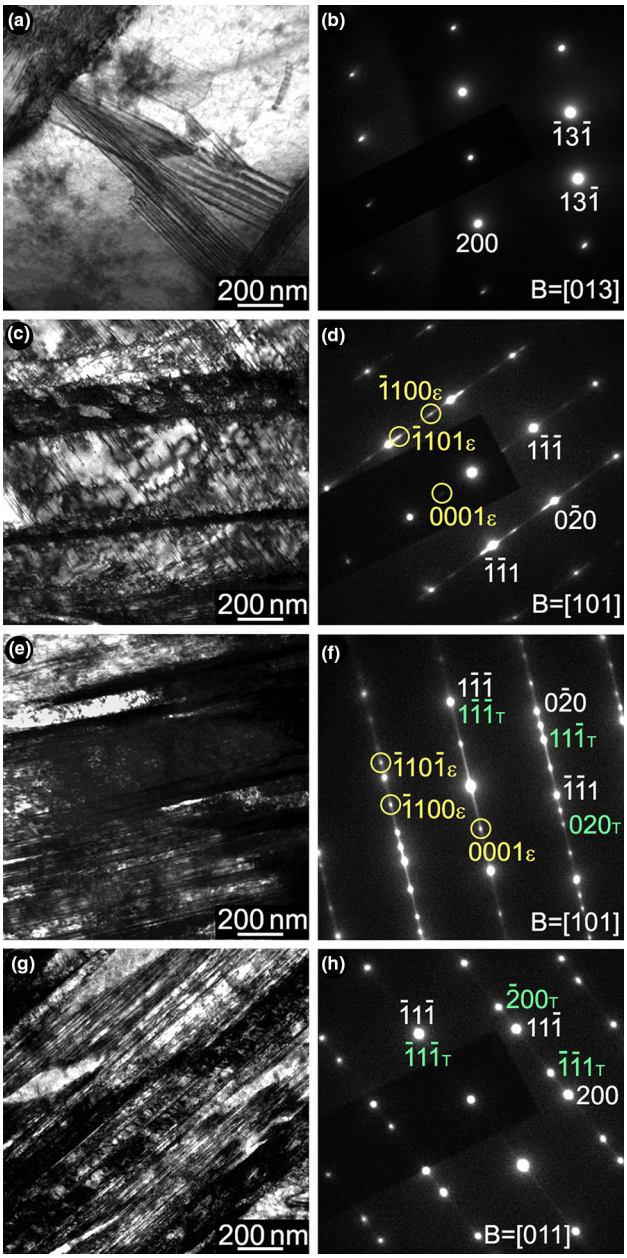

Fig. 7—Representative microstructure developed in austenitic grains: (*a*, *b*) solution-annealed condition, [013]γ zone axis, (*c*, *d*) 10^{-4} s^{-1} tested specimen, [101]γ // [11-20]ε zone axis, (*e*, *f*) 10^{-1} s^{-1} tested specimen, [101]γ // [11-20]ε zone axis, and (*g*, *h*) 10^{1} s^{-1} tested specimen, [011]γ zone axis.

In these alloys, the austenite volume fraction after water quenching was around 50 and 80 pct, respectively, balanced by the presence of α'- and/or ε-martensite. Mcgrath *et al.* reported an initial 27 vol pct of austenite for the composition Fe-15.3Mn-2.85Si-2.4Al-0.07C,[7] while Ding *et al.* informed a 60 vol pct austenite, 35 vol pct α'-, and rest of ε-martensite for the alloy Fe-18.8Mn-2.9Si-2.9Al-0.04C.[8] These compositions agree on a silicon content of 3 wt pct, while the measured content in this contribution is 2.1 wt pct, as shown in Table I. As silicon decreases the γ-austenite stability and sustains the γ/ε transformation upon cooling and deformation, it is expected that a 1 wt pct Si reduction results beneficial for the stabilization of austenite.[3,24] Aluminum addition contributes to austenite stabilization by inhibiting cementite precipitation and consequently favoring the solid solution of carbon in the austenitic matrix.[25,26]

Concerning the deformation mechanism of the alloy, the step-by-step XRD analysis (Figures 2 and 3) confirms the occurrence of the TRIP effect along tensile testing. Particularly, the evolution of the plastic deformation can be described by the two-stage transformation mechanism, $\gamma \rightarrow \varepsilon \rightarrow \alpha'$.[7–9,12] Thus, ε-martensite plates are formed through planes of stacking faults in the austenite at early stage of deformation, explaining the sudden increase of ε-martensite vol pct in the alloy.[27] By increasing plastic deformation, the hcp plates serve for the nucleation and growth of α'-martensite. Consequently, a consumption of the hcp phase takes place upon the increase of α' vol pct. The described mechanism is verified by the EBSD micrograph presented in Figure 6. Consequently, the possibility of a direct transformation of austenite into α'-martensite seems to be unlikely for this alloy.

Certain tendencies of mechanical properties with the applied strain rate can be deduced from the data shown in Table II. First of all, the 0.2 pct offset yield strength (Rp0.2) increases with the strain rate by a 22 pct between 10^{-4} and 10^{1} s^{-1}, in agreement with the results of Grässel and Benzing *et al.* on a Fe-25Mn-3Si-3Al TWIP steel.[3,17] Assuming the absence of martensitic transformation at the 0.2 pct offset, the positive response of Rp0.2 can be related to the effect of the strain rate on the friction stress required for the propagation of dislocations in a crystal lattice, as occurs for stable austenitic steels.[28] On the contrary, the tensile strength (Rm) decreases from 837 to 723 MPa within the 10^{-4} to 10^{1} s^{-1} range. In order to explain this behavior, it is important to note the self-heating process taking place in the specimens due to plastic work. Thus, the increase of temperature can suppress the martensitic transformation and the consequent reduction in the volume fraction of the stronger phase is reflected into a lower material's strength. The same relationship between Rm and strain rate is observed in metastable austenitic steels like 304 and 301LN.[29]

Conclusive information is not available in literature concerning the effect of strain rate on both on uniform elongation (Ag) and elongation to rupture (*A*). In the case of a 309 austenitic stainless steel, where plastic deformation occurs only by dislocations motion and the effect of strain rate can be isolated, an increase on strain rate reduces the uniform elongation between 10^{-6} and 10^{1} s^{-1}.[29] For an Fe-25Mn-3Si-3Al TWIP steel, Grässel *et al.* report a decrease of Ag and *A* for increasing strain rates within the 10^{-4} to 10^{1} s^{-1} interval, while Benzing *et al.* do not distinguish a clear effect of the strain rate upon plasticity.[3,17] In contrast to these results, the HMn-TRIP steel presented here shows an increase of both Ag and *A* with strain rate (see Table II). This result cannot be attributed only to a strain rate effect. Moreover, it responds to a self-heating phenomenon which affects the SFE of the alloy and the

occurring deformation mechanism. This interaction is explained in detail in the following lines.

The changes on mechanical properties suggest that the deformation mechanism of the alloy is somehow affected by increasing strain rates. Such effects become noticeable by observing the slopes of tensile curves in Figure 4, following the evolution of the strain hardening exponent n in Figure 5, and observing the dissimilar phase volume fractions in the specimens after rupture shown in Table III. One outstanding feature along the tensile tests was the temperature rise of the specimens, in agreement with previous reports.[14,17] Therefore, the evolution of temperature was determined *in situ* for the specimens tested at 10^{-4} and 10^{-1} s^{-1} and calculated according to Eq. [2] for the 10^{-1} and 10^{1} s^{-1} loading condition. Equation [2] describes the increase of temperature in the presence of adiabatic heating, as follows[16,30]:

$$\Delta T = \frac{\beta}{\rho C_P} \int_{\varepsilon_1}^{\varepsilon_2} \sigma \partial \varepsilon, \qquad [2]$$

where β is the fraction of mechanical energy converted to heat energy, assumed 0.9, the specific heat capacity is C_P = 0.46 kJ/kg K, typical in steels, and the density ρ = 7.8 g/cm^3. In this regard, Lichtenfeld *et al.* report adiabatic conditions at strain rates higher than 1.25×10^{-1} s^{-1}, while other contributions relate adiabatic heating with strain rates higher than 10^{0} s^{-1}.[29,31,32] The obtained temperature profiles are presented in Figure 8 as a function of engineering strain. As can be seen, the adiabatic heating approach overestimates the actual temperature for the 10^{-1} s^{-1} condition. Therefore, the measured temperature is used hereinafter for the specimens tested at 10^{-4} and 10^{-1}, while calculated values are employed for the 10^{1} s^{-1} strain rate.

All tensile tests were started once the specimen temperature was stabilized with the room temperature set in 22 °C, as shown in Figure 8. While the quasi-static test develops quite close to an isothermal condition, the 10^{-1} and 10^{1} specimens undergo a remarkable increase of temperature. Specifically, the difference between the final and initial temperature results $\Delta T_{(-4)}$ = 3 °C, $\Delta T_{(-1)}$ = 46 °C, and $\Delta T_{(1)}$ = 74 °C for the 10^{-4}, 10^{-1}, and 10^{1} s^{-1} loading condition, respectively. Bearing in mind this increment in temperature with the strain rate, the evolution of the SFE with temperature was assessed since it governs the deformation mechanism occurring in the alloy and it is known to increase with temperature.[33,34]

The SFE as function of temperature can be assessed by the thermodynamic approach proposed by Olson and Cohen, where the SFE is expressed as follows[35]:

$$\mathrm{SFE} = 2\rho\Delta G^{\gamma\to\varepsilon} + 2\sigma^{\gamma/\varepsilon} \qquad [3]$$

being ρ the molar surface density along {111} planes, $\Delta G^{\gamma\to\varepsilon}$ the molar Gibbs free energy of the $\gamma\to\varepsilon$ transformation, and $\sigma^{\gamma/\varepsilon}$ the surface energy of the interface γ/ε. Generally, a value between 5 and 15 mJ/m^2 is adopted for the interface energy $\sigma^{\gamma/\varepsilon}$ when employing Eq. [3].[15,36,37] In this case, an interface energy of $\sigma^{\gamma/\varepsilon}$ = 8 mJ/m^2 was chosen in accordance with the Fe-25Mn-1.6Al-0.24Si TWIP steel, introduced by Curtze and Kuokkala, due to compositional similarities.[16] The difference in Gibbs free energy between the fcc and the hcp phase was calculated by means of a CALPHAD evaluation at − 30, 20, 60, and 120 °C, employing the measured chemical composition of the alloy, see Table I. The calculated values of SFE are presented in Figure 9. By considering the relationship between Figures 7 and 8, it is quite likely that a specimen tested at 10^{-1} and 10^{1} s^{-1} undergoes different SFE values along the same tensile test, while a constant SFE value is expected for the quasi-static testing.

Work hardening behavior as function on strain rate can be associated with the active deformation mechanisms. These mechanisms depend specially on the SFE of the parent austenite phase, which may result in the material evolution from having a pure TRIP effect to a mixed TRIP/TWIP effect.[14] As mentioned in a previous paragraph, the strain hardening exponent n is used as an

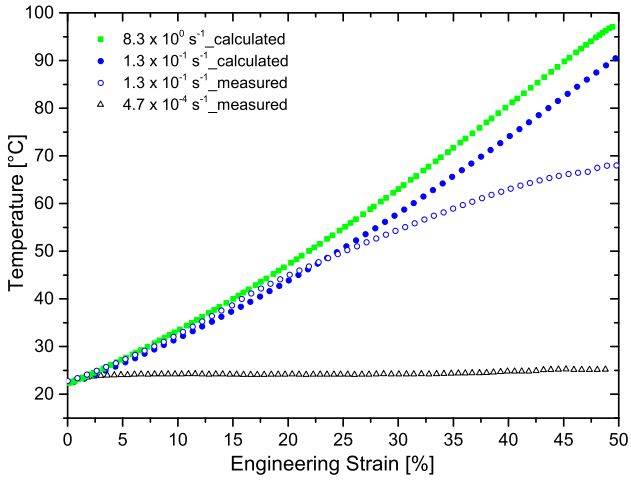

Fig. 8—Evolution of specimens temperature with strain rate. Room temperature was set at 22 °C.

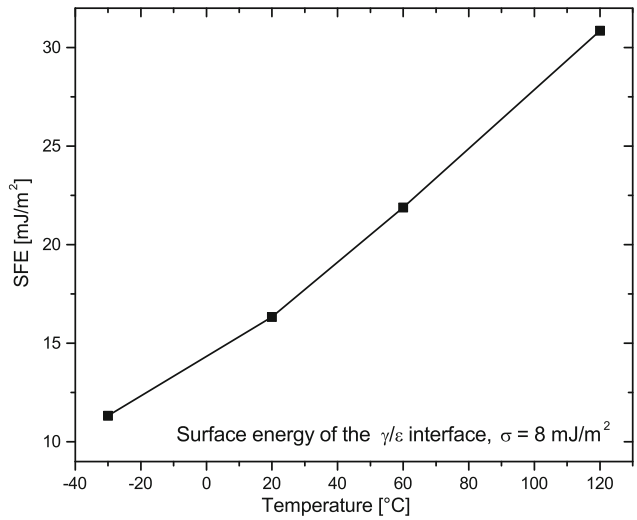

Fig. 9—Calculated values of the SFE after Eq. [3].

indirect measurement of the TRIP effect intensity. Particularly, the maximum n value, n_{max}, is assumed to be representative of the maximum work hardening at a particular instant of time. Therefore, the n_{max} parameter is used for comparison purposes among the investigated strain rate range. Such comparison is summarized in Table IV. Taking the first row of Table IV as an example, it appears that an n_{max} of 0.83 occurs at 25 pct of engineering strain for the 10^{-4} s^{-1} testing condition. This value of engineering strain corresponds to a temperature of 24 °C, see Figure 8, for which, according to Figure 9, the material's SFE has a value of 16.9 mJ/m^2. The same reasoning can be applied in the rest of the cases. Thus, Table IV indicates that, for the instant of maximum hardening, the alloy reaches an SFE of 16.9, 20.5, and 23.4 mJ/m^2 at 10^{-4}, 10^{-1}, and 10^{1} s^{-1} strain rate conditions, respectively.

Taking into consideration the SFE values for the maximum hardening instant, a comparison among the occurring deformation mechanism in each case can be made. The value of 16.9 mJ/m^2 encountered for the 10^{-4} condition is related to the activation of martensitic strain-induced transformations in this kind of steels.[5,7,13,34] On the other hand, a SFE value higher than 18 mJ/m^2 is required to activate TRIP/TWIP effect with substantial contribution of both mechanisms.[38,39] That is precisely the condition of the 10^{-1} and 10^{1} s^{-1} specimen at maximum strain hardening. Therefore, with the activation of the TWIP mechanism, a lower slope in the tensile curve and a higher elongation to fracture is expected, together with a lower amount of strain-induced martensite formation.[3–5,39] This is actually observed in Figure 4 and Table III.

The TEM micrographs shown in Figure 7 provide evidence of the activation of TWIP phenomenon for specimens tested at 10^{-1} and 10^{1} s^{-1} strain rate conditions. This is in correspondence with the relationship between strain rate, temperature, calculated SFE, and the mechanical behavior exhibited by the alloy.

The decisive influence of temperature in the resulting deformation mechanism motivated the determination of the Md temperature of the alloy, *cf.* Section II–C. In that manner, a Md = 36.3 °C was obtained as shown in Figure 10. Below Md, the yield stress–temperature exhibits a positive slope in correspondence with the presence of strain-induced martensite formation (*i.e.* a Clausius–Clapeyron relationship). Above Md, the change in the yield stress *vs* temperature slope, from an ascendant slope to a descendent slope, indicates a change in the governing deformation mechanism from the two-stage $\gamma \rightarrow \varepsilon \rightarrow \alpha'$ to other mechanism controlled, in this case, mainly by twinning (twinning is energetically favored just above Md over dislocation motion, while dislocation slip becomes predominant at higher temperatures[16]).

From Figure 10, Md is determined as 36.3 °C. According to the relationship between SFE and temperature displayed in Figure 9, this temperature corresponds to an SFE value of 18.6 mJ/m^2. By overcoming this level, twinning takes over from martensitic transition as the plasticity controlling mechanism. This fact highlights the significance of determining the Md value of the alloy under study. By knowing Md and calculating the adiabatic temperature rise with Eq. [2], the behavior of the alloy could be estimated over the working temperature range. For instance, an alloy with Md close to room temperature can bring about the most beneficial strength–elongation by taking advantage of the transition between ε-martensite transformation and twinning.

Finally, it is worth to note that the EAC of the alloy is slightly affected by the strain rate. Particularly, the product between Rm and A indicates a reduction of 3.6 pct between the highest and lowest values expressed in MPa pct, see Table II.

V. CONCLUSION

The mechanical behavior and microstructural evolution of a laboratory cast austenitic Fe-18Mn-2Si-2Al TRIP steel was studied under tensile loading from

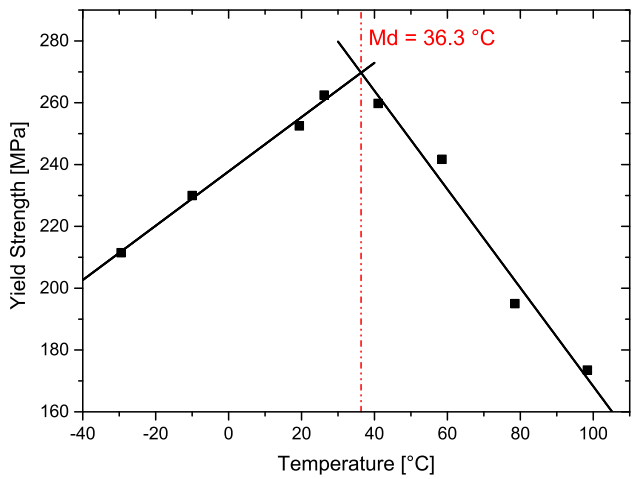

Fig. 10—Md temperature determination. Yield strength plotted as function of temperature for specimens tested at quasi-static condition, 10^{-4} s^{-1}.

Table IV. Correlation Between Strain Rate, Specimen's Temperature, and SFE at Maximum Strain Hardening Exponent, n_{max}

Strain Rate (1/s)	n_{max}	Engineering Strain (Pct)	T (°C)	SFE (mJ/m^2)
4.7×10^{-4} (10^{-4})	0.83	25	24	16.9
1.3×10^{-1} (10^{-1})	0.63	25	50	20.5
8.3×10^{0} (10^{1})	0.65	32	70	23.4

SFE values obtained out of Fig. 9.

quasi-static to low-dynamic regime in three levels of strain rate: 4.7×10^{-4}, 1.3×10^{-1}, and 8.3×10^{0} s^{-1}. Within this loading range, yield stress increases with strain rate, tensile strength decreases with strain rate, and ductility increases for both uniform elongation, Ag, and elongation to rupture, *A*. The higher work hardening at the quasi-static condition is attributed to a two-stage transformation mechanism, $\gamma \rightarrow \varepsilon \rightarrow \alpha'$, which develops isothermally and is verified by XRD and TEM analysis. This finding is in accordance with a calculated SFE value of 16.9 mJ/m^2, using the CALPHAD method.

For the higher strain rates, 1.3×10^{-1} and 8.3×10^{0} s^{-1}, the temperature rise due to adiabatic heating is high enough to shift the SFE above 18 mJ/m^2 and consequently introduce the alloy into a mixed zone where both TRIP/TWIP mechanisms can occur. This shifting in the deformation mechanism is supported by lower slopes in the tensile curves and higher amounts of untransformed austenite. The additional presence of the TWIP effect is responsible of the higher ductility of the alloy at higher strain rates. The temperature rise in the specimen, during mechanical testing, overcomes the Md temperature of the alloy. The complex interplay between temperature, strain rate, and SFE on the TRIP, TWIP, and other hardening mechanisms highlights the need of controlling Md temperature in the design of this kind of alloys.

Finally, the EAC of the alloy is reduced by only a 3.6 pct in the mentioned strain rate regime.

ACKNOWLEDGMENTS

The authors acknowledge the support of CONICET Argentina under Grants PUE096-IFIR and PDTS-251. As well, the contribution of Professor Dr.-Ing. Lais Mujica Roncery, Universidad Pedagógica y Tecnológica de Colombia, on thermodynamic calculations, and the support of Dr. Laura Buttigliero, IFIR-CONICET, by TEM characterization are acknowledged.

REFERENCES

1. B.C. De Cooman, K. Chin, and J. Kim: in *New Trends and Developments in Automotive System Engineering*, M. Chiaberge, ed., InTech, London, 2011, pp. 101–28.
2. H. Hofmann, D. Mattissen, and T.W. Schaumann: *Materwiss. Werksttech.*, 2006, vol. 37, pp. 716–23.
3. O. Grässel, L. Krüger, G. Frommeyer, and L.W. Meyer: *Int. J. Plast.*, 2000, vol. 16, pp. 1391–409.
4. O. Grässel, G. Frommeyer, and C. Derder: *J. Phys. IV*, 1997, vol. 07, pp. C5-383–88.
5. G. Frommeyer, U. Brüx, and P. Neumann: *ISIJ Int.*, 2003, vol. 43, pp. 438–46.
6. A. Sato, K. Soma, and T. Mori: *Acta Metall.*, 1982, vol. 30, pp. 1901–07.
7. M.C. Mcgrath, D.C. Van Aken, N.I. Medvedeva, and J.E. Medvedeva: *Metall. Mater. Trans. A*, 2013, vol. 44A, pp. 4634–43.
8. H. Ding, H. Ding, D. Song, Z. Tang, and P. Yang: *Mater. Sci. Eng. A*, 2011, vol. 528, pp. 868–73.
9. S.S.F. de Dafé, F.L. Sicupira, F.C.S. Matos, N.S. Cruz, D.R. Moreira, and D.B. Santos: *Mater. Res.*, 2013, vol. 16, pp. 1229–36.
10. L. Bracke, L. Kestens, and J. Penning: *Scripta Mater.*, 2007, vol. 57, pp. 385–88.
11. S.T. Pisarik and D.C. Aken: *Metall. Mater. Trans. A*, 2016, vol. 47A, pp. 1009–18.
12. W.Y. Jang, Q. Gu, J. Van Humbeeck, and L. Delaey: *Mater. Charact.*, 1995, vol. 34, pp. 67–72.
13. D.T. Pierce, J.A. Jimenez, J. Bentley, D. Raabe, C. Oskay, and J.E. Wittig: *Acta Mater.*, 2014, vol. 68, pp. 238–53.
14. D.T. Pierce, J.A. Jimenez, J. Bentley, D. Raabe, and J.E. Wittig: *Acta Mater.*, 2015, vol. 100, pp. 178–90.
15. S. Allain, J.P. Chateau, O. Bouaziz, S. Migot, and N. Guelton: *Mater. Sci. Eng. A*, 2004, vols. 387–389, pp. 158–62.
16. S. Curtze and V.T. Kuokkala: *Acta Mater.*, 2010, vol. 58, pp. 5129–41.
17. J.T. Benzing, W.A. Poling, D.T. Pierce, J. Bentley, K.O. Findley, D. Raabe, and J.E. Wittig: *Mater. Sci. Eng. A*, 2018, vol. 711, pp. 78–92.
18. H.M. Rietveld: *J. Appl. Crystallogr.*, 1969, vol. 2, pp. 65–71.
19. L. Lutterotti, S. Matthies, H.R. Wenk, A.S. Schultz, and J.W. Richardson: *J. Appl. Phys.*, 1997, vol. 81, pp. 594–600.
20. S. Xu, D. Ruan, J.H. Beynon, and Y. Rong: *Mater. Sci. Eng. A*, 2013, vol. 573, pp. 132–40.
21. I. Gutierrez-Urrutia and D. Raabe: *Acta Mater.*, 2011, vol. 59, pp. 6449–62.
22. P. Kürnsteiner, C. Commenda, E. Arenholz, L. Samek, D. Stifter, and H. Groiss: *Materialia*, 2018, vol. 1, pp. 70–7.
23. S. Pramanik, A.A. Gazder, A.A. Saleh, and E.V. Pereloma: *Mater. Sci. Eng. A*, 2018, vol. 731, pp. 506–19.
24. R.E. Schramm and R.P. Reed: *Metall. Trans. A*, 1975, vol. 6, pp. 1345–51.
25. B.K. Zuidema, D.K. Subramanyam, and W.C. Leslie: *Metall. Mater. Trans. A*, 1987, vol. 18A, pp. 1629–39.
26. W.C. Leslie and G.C. Rauch: *Metall. Mater. Trans. A*, 1978, vol. 9A, pp. 343–49.
27. F. Lu, P. Yang, L. Meng, F. Cui, and H. Ding: *J. Mater. Sci. Technol.*, 2011, vol. 27, pp. 257–65.
28. S.V. Astafurov, G.G. Maier, E.V. Melnikov, V.A. Moskvina, M.Yu. Panchenko, and E.G. Astafurova: *Mater. Sci. Eng. A*, 2019, vol. 756, pp. 365–72.
29. J.A. Lichtenfeld, M.C. Mataya, and C.J. Van Tyne: *Metall. Mater. Trans. A*, 2006, vol. 37A, pp. 147–61.
30. W.-S. Lee, G.-L. Xiea, and C.-F. Lin: *Mater. Sci. Eng. A*, 1998, vol. 257, pp. 256–67.
31. P. Dixon and D. Parry: *J. Phys. IV*, 1991, vol. 01, pp. 85–92.
32. S. Klitschke, A. Trondl, F. Huberth, and M. Liewald: *IOP Conf. Ser. Mater. Sci. Eng.*, 2018, https://doi.org/10.1088/1757-899X/418/1/012123.
33. L. Remy: *Acta Metall.*, 1977, vol. 25, pp. 173–79.
34. O.A. Zambrano: *J. Eng. Mater. Technol.*, 2016, vol. 138, p. 041010.
35. G.B. Olson and M. Cohen: *Metall. Trans. A*, 1976, vol. 7, pp. 1897–1904.
36. P.J. Ferreira and P. Müllner: *Acta Mater.*, 1998, vol. 46, pp. 4479–84.
37. Y.K. Lee and C.S. Choi: *Metall. Mater. Trans. A*, 2000, vol. 31A, pp. 355–60.
38. J. Kim and B.C. De Cooman: *Mater. Sci. Eng. A*, 2016, vol. 676, pp. 216–31.
39. F. Berrenberg, C. Haase, L.A. Barrales-mora, and D.A. Molodov: *Mater. Sci. Eng. A*, 2016, vol. 681, pp. 56–64.